small methods
www.small-methods.com

Applications of X-Ray-Based Characterization in MXene Research

Jizhen Zhang, Ken Aldren S. Usman, Mia Angela N. Judicpa, Dylan Hegh, Peter A. Lynch, and Joselito M. Razal**

X-rays are a penetrating form of high-energy electromagnetic radiation with wavelengths ranging from 10 pm to 10 nm. Similar to visible light, X-rays provide a powerful tool to study the atoms and elemental information of objects. Different characterization methods based on X-rays are established, such as X-ray diffraction, small- and wide-angle X-ray scattering, and X-ray-based spectroscopies, to explore the structural and elemental information of varied materials including low-dimensional nanomaterials. This review summarizes the recent progress of using X-ray related characterization methods in MXenes, a new family of 2D nanomaterials. These methods provide key information on the nanomaterials, covering synthesis, elemental composition, and the assembly of MXene sheets and their composites. Additionally, new characterization methods are proposed as future research directions in the outlook section to enhance understanding of MXene surface and chemical properties. This review is expected to provide a guideline for characterization method selection and aid in precise interpretation of the experimental data in MXene research.

1. Introduction

Recently, MXenes, or transition metal carbides/nitrides ($M_{n+1}X_nT_x$, where M = transition metal, X = carbon/nitrogen, and T_x = –OH, –F or –O) have gained tremendous research interest for their unique combination of high conductivity (up to 24 000 S cm^{-3})[1,2] and volumetric capacitance (>1500 F cm^{-3}).[3,4] This desirable blend of properties has made MXenes attractive for a plethora of applications including, but not limited to, energy storage,[5,6] conductive transparent electrodes,[7–10] field effect transistors,[11] and electromagnetic interference (EMI) shielding.[12] MXenes also boast unique hydrophilicity due to hydroxyl or oxygen terminated surfaces resulting in colloidal stability.[13] The growing understanding of their rheological behavior[14,15] and dispersibility in a variety of polar organic solvents[13,16,17] has enabled the fabrication of high performance functional architectures and geometries such as fibers[15] and porous 3D-structures,[18] giving access to practical applications.

MXenes are generally synthesized by selectively etching the aluminum layers of precursors known as MAX phases (**Figure 1**a).[19–21] Starting from etching and delamination of a parent MAX phase, up to the fabrication of functional structures and composites, a number of advanced characterizations are necessary to assess the structural and chemical properties of MXenes. For example, imaging techniques like scanning electron microscopy (SEM) and atomic force microscopy (AFM) aid in validating the success of chemical etching. Through SEM, it can be confirmed that the solid MAX phase particles transform into layer structures, indicating the production of multilayer or few-layer MXene sheets (Figure 1b,c).[4,22,23] Further imaging techniques such as transmission electron microcopy (TEM), selected area electron diffraction (SAED), and electron energy loss spectroscopy (EELS)[24–27] may also be utilized. TEM not only confirms the formation of MXene flakes, but its high-resolution imaging in tandem with SAED is also able to verify the atomic arrangement, spacing, and presence of defects in the structure of the nanosheets (Figure 1d).[4,22,23] The thickness of the fully delaminated nanosheets is then usually quantified through AFM.[28–31] AFM and SEM can also be used in tandem to corroborate the quality of $Ti_3C_2T_x$ MXene, synthesized with and without sonication, by comparing its sheet size and thickness (Figure 1e–h).[31] Early demonstrations of this approach also aided the development of the minimally intensive layer delamination method for MXene synthesis.[20]

The research on processing MXene films,[32] fibers,[4,33] coatings,[34] and aerogels[35] also benefits from advanced characterization techniques. For example, elemental mapping methods

J. Zhang, K. A. S. Usman, M. A. N. Judicpa, D. Hegh, P. A. Lynch, J. M. Razal
Institute for Frontier Materials
Deakin University
Geelong, VIC 3216, Australia
E-mail: k.usman@deakin.edu.au; joselito.razal@deakin.edu.au
J. Zhang, P. A. Lynch
Manufacturing
Commonwealth Scientific and Industrial Research Organization (CSIRO)
Waurn Ponds, VIC 3216, Australia

The ORCID identification number(s) for the author(s) of this article can be found under https://doi.org/10.1002/smtd.202201527

DOI: 10.1002/smtd.202201527

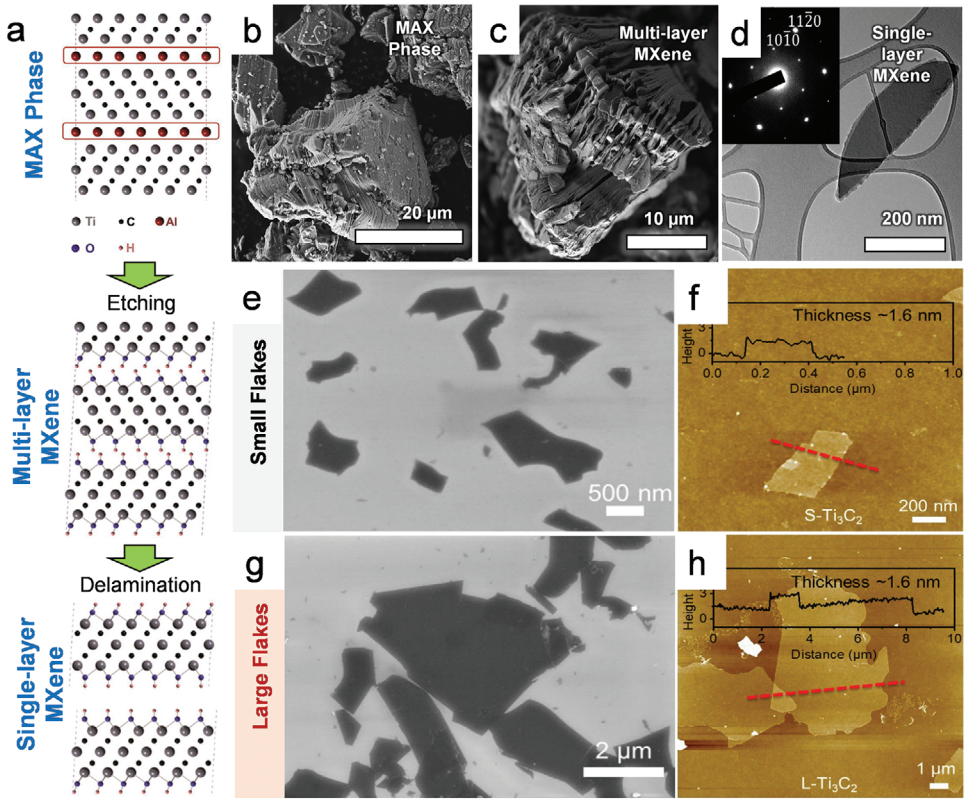

Figure 1. a) The scheme of MXene synthesis from MAX phase to multilayer MXene and single-layer MXene. Reproduced with permission.[23] Copyright 2011, Wiley-VCH GmbH. SEM images of b) Ti_3AlC_2 MAX phase and c) ml-MXene. d) TEM image of a delaminated MXene. The inset in (d) is the selected area electron diffraction (SAED) pattern of the flake. Reproduced with permission.[22] Copyright 2017, The Royal Society of Chemistry. e–h) Effect sonication on MXene morphology visualized through SEM and AFM. Reproduced with permission.[31] Copyright 2020, Wiley-VCH GmbH.

such as energy dispersive X-ray spectroscopy (EDX/EDS) illustrate sheet-stacking in a composite, as well as the distribution of intercalated electrolyte materials in films when assembled into functional devices such as a supercapacitor.[32] Additionally, complementary methods such as Fourier-transform infrared spectroscopy and thermogravimetric analysis have been utilized to understand the surface groups functionalizing MXene and its composites.[36–38]

In general, the physical properties of nanomaterials are closely dependent on their atom arrangements and crystal structure stability.[39] Additionally, achieving functionality in practical applications also calls for intricate design of materials at a molecular level (e.g., elemental modification) prior to processing into architectures.[39] Investigation of such properties requires characterization methods with high level of spatial resolution, sensitivity, and nondestructibility, which cannot be offered by the typical electron-microscopy and bench-top chemical characterization methods. In this regard, X-ray-based techniques show high relevance for quite a few reasons.

X-rays are a form of high-energy electromagnetic radiation, with wavelengths ranging from 10 pm to 10 nm, corresponding to frequencies ranging from 30 PHz to 30 EHz and energies from 145 eV to 124 keV, respectively. Its small wavelength allows passage through most substrates to reveal detailed structural information. After over a hundred years of development, X-ray-based techniques, such as X-ray diffraction (XRD), X-ray fluorescence analysis, and small- and wide-angle scattering of X-rays (SAXS/WAXS), have become crucial components of materials science. In particular, they serve as powerful nondestructive means of characterizing crystalline materials.[40] Although these characterization methods utilize X-rays, their respective working mechanisms provide vastly different material information. Some techniques give insight on structures, phases, preferred crystal orientations (texture), and other structural parameters, such as average grain size, crystallinity, strain, and crystal defects.[39,40] The other capabilities provide information about the core electron of a given material, allowing quantification of almost all elements, as well as insights about their orbital states and chemical bonds.[41–43]

In this review, we provide an overview of different state-of-art X-ray methods and how these have advanced MXene research. We introduce the fundamental principles and approaches developed for qualitative and quantitative characterization of MXenes using widely utilized X-ray-based techniques, including XRD,[19,22,44] SAXS/WAXS,[15,30,31,33,45] X-ray photoelectron spectroscopy (XPS),[42,46,47] X-ray absorption spectroscopy (XAS),[48–50] and X-ray imaging (micro-computed tomography or micro-CT).[51] Our discussions focus on the key information provided via each technique, with emphasis on how they contribute to the fundamental understanding and development of MXenes toward an array of applications. As an outlook, the limitations and unexplored capabilities of each X-ray technique are openly

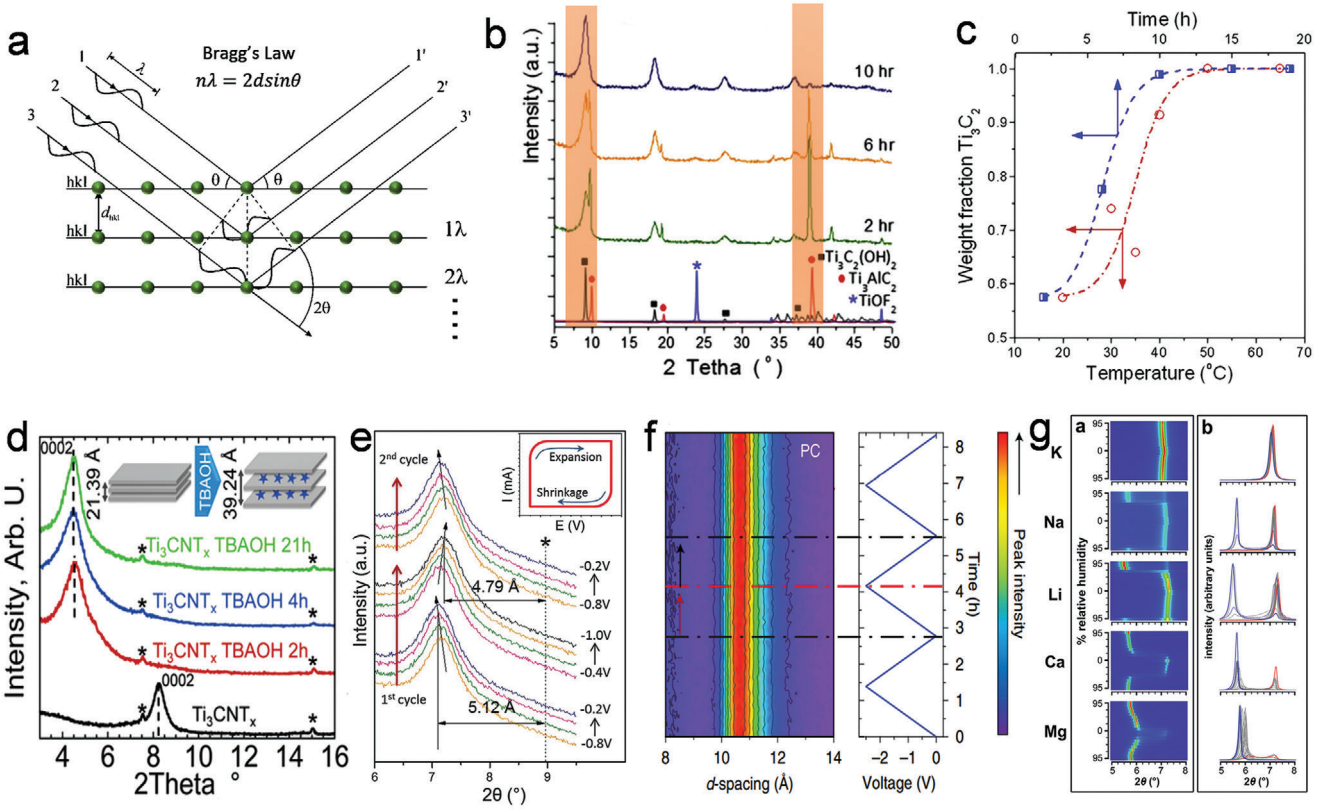

Figure 2. a) Scheme of X-ray wave interference and Bragg's law. b) XRD patterns obtained after etching Ti_3AlC_2 powders in 50% HF at RT as a function of time, peak changes highlighted. c) Effect of temperature (red, bottom *x*-axis) and time (blue, top *x*-axis) on exfoliation kinetics. Reproduced with permission.[58] Copyright 2013, Elsevier Ltd. d) Ti_3CNT_x before (black) and after mixing with TBAOH for 2, 4, and 21 h (red, blue, and green). Reproduced with permission.[61] Copyright 2015, Royal Society of Chemistry. e) Electrochemical in situ XRD study of multilayer $Ti_3C_2T_x$ exfoliated in 1 M KOH. Reproduced with permission.[62] Copyright 2013, American Association for the Advancement of Science. f) In situ XRD map of vacuum-filtered Ti_3C_2 in PC-based electrolyte during charging and discharging. Reproduced with permission.[63] Copyright 2019, Springer Nature Ltd. g) 3D plots of the (002) region of A-$Ti_3C_2T_x$ (with each intercalated cation A denoted at left) as RH was varied from 95% to ≈0 and back to 95%. The color scheme represents diffraction intensity, red is highest, blue is lowest. Reproduced with permission.[64] Copyright 2016, American Chemical Society.

discussed to provide a reference for extending the prospects of X-ray techniques in MXene studies.

2. X-Ray Techniques in MXene Research

Depending on the characterization technique, X-rays are utilized either as an energy source used to illuminate the sample (e.g., XRD, XPS) or as the signal emitted by the sample itself (e.g., EDX). The following sections highlight the breadth and depth of X-ray methods and how these have enabled extensive research on MXenes. The methods are categorized based on the type of information they produce, such as crystallinity, chemical profile, and micro/macrostructural information of MXenes and their composites.

2.1. Crystal Information from X-Ray Diffraction

XRD is a powerful technique for determining the crystallographic information of materials, including cell parameters,[52] strain,[53] and microstructural information,[54] and it has been widely applied in material studies.[19,55,56] XRD uses monochromatic radiation that is generated by a cathode ray tube. The interaction of the incident rays with the sample produces constructive interference and, subsequently, a diffracted ray when conditions satisfy Bragg's law ($n\lambda = 2d\sin\theta$) (**Figure 2**a).[55] By measuring the angle between the incident and scattered X-rays, the *d*-spacing between atomic planes of a crystal can be obtained. For 2D nanomaterials, this is referred to as *c*-lattice parameter (*c*-LP) and describes the spacing between parallel neighboring nanosheets. The use of XRD in monitoring the changes in *c*-LP of MXenes has been massively used in its synthesis, composites fabrication, and materials assessment for different applications.

Since MXenes are synthesized by selectively etching intercalated atom layers from their parent materials (MAX phases), monitoring the XRD patterns can reveal the progress of etching and prove the exfoliation of MXene sheets.[19] Two important changes observed in the MAX phase XRD pattern after etching are: i) the appearance of a (002) peak at low 2θ angles (normally lower than 10°), which is related to the increase in *c*-LP constant after removal of intercalated layers, and ii) the decrease or disappearance of peaks attributed to the intercalated layers, located at 2θ of ≈40° (Figure 2b). Although XRD patterns can prove the formation of MXenes,[21,57] it is critical to quantify such data when studying the etching rate and yield. Mashtalir et al.[58]

showed that XRD calibration can be undertaken using mixtures with known ratios of pure MXene and the original MAX phase as standard samples to demonstrate the effect of time and temperature on MXene yield (Figure 2c). Additionally, the etching of "A" layers from MAX phase results in multilayer structures due to the strong H-bonding induced stacking between individual sheets. Complete delamination into single-layer MXene requires additional steps to increase the layer spacing at nanometer scale.[20,21,59] Hence, XRD provides an effective approach to monitor changes in the layer spacing for increased yield of single-layer MXenes.[60] For example, Naguib et al.[61] found that treating Ti_3CNT_x with the intercalant tetrabutylammonium hydroxide (TBAOH) for 2 h caused a significant shift in the (002) peak from 2θ of 8.26° to 4.57° (Figure 2d). This shift corresponds to a *c*-LP increase from 21.4 to 38.6 Å. After 4 h of mixing, the (002) peak shifted to 2θ of 4.5° corresponding to a *c*-LP of 39.2 Å. These observations proved that small molecules infiltrate between MXene sheets, which led to establishing the general approach of weakening the bonds between MXene layers being necessary for large-scale delamination.

Besides traditional XRD experiments, an in situ XRD approach has enabled structural studies of MXene undergoing chemical reactions or processing. For example, in situ XRD studies on $Ti_3C_2T_x$ electrode in KOH-containing electrolyte showed insignificant changes in *c*-LP values of 0.33 Å during electrochemical cycling (−1 to −0.2 V) (Figure 2e).[62] The simplest explanation for this observation is that the positively charged ions incorporated in $Ti_3C_2T_x$ increase interlayer electrostatic attraction. In comparison with reversible and continuous shifts, Mu et al.[65] found through in situ XRD studies that the mechanism of H^+ intercalation appears to be more complex. Both shrinkage and expansion of the *c*-LP during a single charge or discharge were observed, and a simulation study showed that H^+ intercalation tends to shrink the interlayer space of O-terminated MXenes but expands the space for OH-terminated MXenes.[65] Moreover, the *c*-LP increased 0.54 Å during this single cycle, which is a substantial change compared with other aqueous electrolytes previously studied. H^+ is a smaller cation than the others tested (Na^+, Mg^{2+}, and K^+). Although all of them insert into the MXene interspaces in their partially hydrated form, the large increase in *c*-LP that occurred for H^+ suggested a large amount of intercalated H^+. This intercalation explains why the capacitance of $Ti_3C_2T_x$ in H_2SO_4 is the highest. In situ XRD measurements have also illustrated the evolution of interlayer space in $Ti_3C_2T_x$ electrodes cycled in organic electrolytes such as dimethyl sulfoxide (DMSO), acetonitrile, and propylene carbonate (PC).[63,66] Uniquely, the $Ti_3C_2T_x$ *d*-spacing in PC electrolyte remained constant (10.7 Å) during cycling (Figure 2f), while the *d*-spacing for the DMSO system varied between 18.8 and 19 Å.[63] These results demonstrate that matching the electrolyte composition to the electrode material is essential for controlling the charge-storage mechanism in order to achieve superior electrochemical performance.

Beyond the above applications, in situ XRD was also used to monitor unit cell expansion in response to humidity changes and hydration heterogeneity (Figure 2g). Expansion was shown to be dependent on the intercalated cation, with *d*-spacing changes consistent with the size of H_2O.[64] Hydration heterogeneity and related structure disorder are described from the quantitative analysis of X-ray diffraction data. XRD experiments under different relative humidity (RH) conditions were performed on oriented MXene films. Experimental XRD patterns reported by Ferrage and co-workers[67] showed a shift of the main diffraction peak from ≈15.9 to ≈12.4 Å on decreasing RH. These two peaks correspond to the 001 reflection of bihydrated (2 W) and monohydrated (1 W) MXenes, respectively. The transition between the two hydration states occurring over the 60–45% RH range, but 1 W layers remains at high RH conditions of 95%. Another research was carried out by thermal annealing the MXene films to trace the deintercalation of water molecules. Ex situ XRD showed a contraction of the *c*-LPs of $Ti_3C_2T_x$ and Ti_3CNT_x (signifying decrease in the interlayer spacing) after respectively annealing at 200 and 150 °C,[37] which further confirms the partial deintercalation of water and supports the argument that deintercalation improves conductivity through a reduced interflake resistance.[37] However, the interstratification phenomenon is still not been well studied enough in the field of MXenes, leading to contrasted layer-to-layer distances but also segregation in a same crystal. The interstratification leads to coexistence of several (002) peaks on the XRD pattern or shoulders of (002) peaks, or shift of peaks, etc. Therefore, the sample preparation methods, drying method, solvent type, environment humidity, and cations concentrations should be labeled properly by researchers to help others understand the XRD data.

XRD has also contributed to the study of MXene-based composites by revealing that the *c*-LP changes after assembly, with increases in *c*-LP as evidence of alternate MXene-additive stacking and/or homogenous distribution of MXene sheets.[22,44] This was first demonstrated by mixing MXene with polymers, such as poly(diallyldimethylammonium chloride) and polyvinyl alcohol. With increasing PVA loading, the (002) peak shifted from 6.0° to 4.8°, equivalent to an increase in *c*-LP. A concomitant increase in full width at half maximum indicated an increasing, but less uniform distance between the individual $Ti_3C_2T_x$ flakes.[32] Although easy access and sample preparation, as well as rapid testing procedures, are among the key advantages of XRD, it is not sensitive enough to detect minimal chemical and/or chemical changes in MXene sheets. For example, the early stages of oxidation that occur at the edge of MXene cannot be distinguished by XRD (but can be detected with Raman spectroscopy or XPS).[39,68,69]

2.2. Chemical Profiling of MXene

2.2.1. XPS

XPS, also referred to as electron spectroscopy for chemical analysis (or ESCA), is a quantitative elemental analysis capable of providing details about the bonding and oxidation state of elements present at the material surface.[42,70,71] Usually done under high vacuum ($<10^{-7}$ Pa), photoelectrons are ejected from the core or valence band of atoms in a sample (**Figure 3**a) by an incident X-ray, typically using Mg as source.[71] The energy of the emitted photoelectrons, which is definite for every element, provides sensitive fingerprint information about the atoms present at a sample surface, including any energy difference that may imply existing chemical bonds or changes in their current oxidation states.

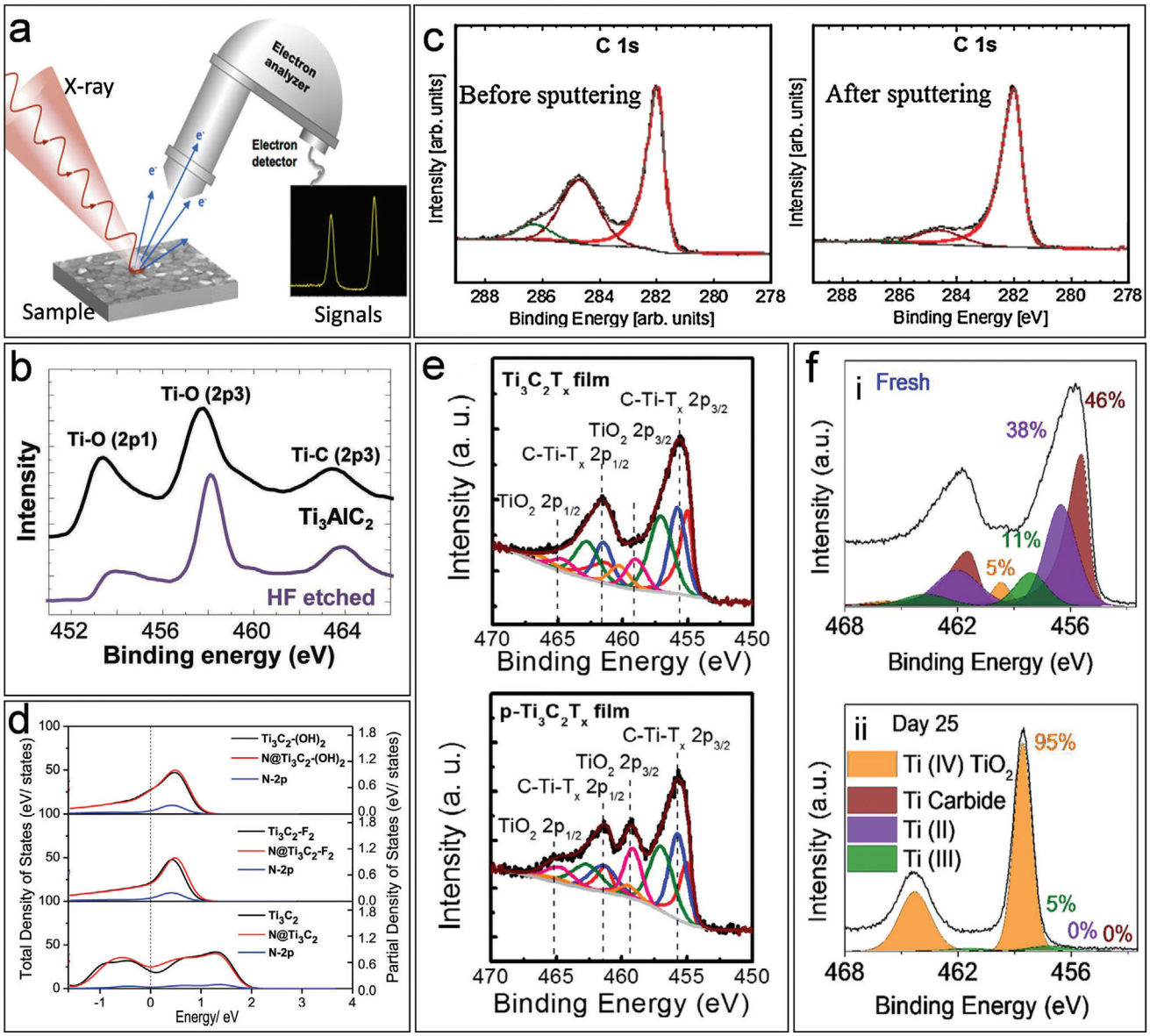

Figure 3. a) Scheme of a typical data collection process of XPS analysis. Reproduced with permission.[71] Copyright 2020, Elsevier Ltd. b) The Ti 2p spectra of the first use of XPS to verify the synthesis of $Ti_3C_2T_x$ MXene. Reproduced with permission.[23] Copyright 2011, Wiley-VCH GmbH. c) Effect of sputtering on the C 1s spectra of MXene. Reproduced with permission.[42] Copyright 2016, Elsevier Ltd. d) DFT simulations using XPS data as input in order to identify how MXene interacted with a N-rich dopant. Reproduced with permission.[81] Copyright 2017, Elsevier Ltd. e) Comparison between the Ti 2p spectra of pristine and modified MXene. Reproduced with permission.[83] Copyright 2016, Wiley-VCH GmbH. f) The use of Ti 2p core spectra to monitor MXene oxidation. Reproduced with permission.[69] Copyright 2017, Wiley-VCH GmbH.

The ability of XPS to characterize both the elemental and chemical structures of surfaces makes it particularly useful, as it can also be used to analyze virtually any form of material.[70]

The first MXene article published by Naguib et al.[23] heralded the importance of XPS for confirming successful MAX phase etching, as this technique can be used to monitor the removal of the Ti–Al bond through HF etching. Moreover, the relative increase in Ti–O $2p^3$ bond intensity confirmed the formation of hydroxyl and/or oxide functional groups on the MXene surface, hence the addition of T_x to its chemical notation (Figure 3b). The elucidation of these surface terminations has been particularly crucial in understanding their excellent colloidal stability and processability.[13,14] Since then, the use of XPS in MXene research has advanced significantly. XPS is commonly used in MXene studies for i) quantitative elemental profiling in pristine and/or doped MXenes,[46,47,72,73] ii) characterization of surface chemistry, including changes in surface functionalization and interfacial interactions,[45,74,75] and iii) assessment of chemical stability through monitoring of oxidation products.[69,76,77] Notably, the purpose of using XPS in MXene studies is not always based on just one of the above reasons, but may hinge on an overlap of two or three.

XPS has been a go-to-characterization technique for accurate identification of atomic composition of MXenes from their MAX phase precursors.[2] For instance, the recent work of Mathis et al.,[2] which provides insights on improving the quality and properties of MXenes through modified MAX phase synthesis, heavily utilized XPS analysis to identify the stoichiometry of acquired MAX precursors. They found that excess aluminum led to Ti_3AlC_2 grains with improved crystallinity and carbon stoichiometry, resulting in MXenes with enhanced chemical stability and conductivity up to 20 000 S cm^{-1}. This high sensitivity of XPS also allowed detection of hitherto unseen impurities brought about by typical handling of samples. For instance, Halim et al.[42] observed how Ar^+ sputter cleaning of various pristine MXene surfaces led to less impurities, implied by the lower intensity of the ≈285 eV peak of its C 1s spectra compared to untreated samples (Figure 3c). Acquiring cleaner sample surfaces also advanced the understanding of MXene's surface terminations. This study confirmed that MXenes with higher number of "M–X" layers possess higher –O to –OH ratio while the presence of mixed "X" (combined C–N) in the multilayer structure counteracts this effect. The ability to predict MXene surface terminations has impacted the selection and tailoring of its applications (e.g., lithium storage prefers MXenes rich in O groups[78]).

The XPS-derived compositional profiles have also been used as input data for follow-up analyses such as DFT calculations.[79,80] These studies have improved the correlation among chemical structure, physical properties, chemical stability, and/or electrochemical performances.[42] As an example, DFT calculations using the elemental composition (from XPS) of nitrogen-doped MXene have provided insights into how N-dopants could interact with MXene (Figure 3d).[81] In follow up studies, interactions such as surface adsorption, functional substitution, and lattice substitution led to correlation between doping and electrochemical capacitance.[79]

In addition to typical elemental analysis, XPS is highly sensitive to detect atomic bonding interactions by analyzing the Ti 2p, O 1s, C 1s, and F1s core spectra. XPS studies of MXene composites allow the investigation of interactions between polymers (e.g., polydopamine,[45] cellulose,[30] alginate[82]) and MXenes. The covalent or electrostatic interactions implied through shifts in binding energy derived from the Ti 2p and O1s core spectra provide insights into possible reinforcement mechanisms in composites.

The detection of oxidation states through XPS also allows quality assessment of MXene and its composites. As the MXene transition metal is crucial for its redox behavior, the absence of its corresponding oxide peak (e.g., TiO_2 in $Ti_3C_2T_x$) is often used as a benchmark of MXene quality. This technique resulted in several efforts to optimize synthetic procedures toward high-quality MXenes, with properties tailored to satisfy the requirements of several applications.[76,83] As an example, XPS analysis of porous p-$Ti_3C_2T_x$ films confirmed the low intensity of TiO_2 peaks (Figure 3e) even after partial oxidation with O_2/H_2O and Cu^{2+} and HF washing, implying these conditions did not significantly affect the chemical composition of MXenes. Identifying the presence of oxidized transition metals through XPS has also become useful in determining the optimum storage conditions for MXene.[17,69,76,77,84,85] For example, XPS provided conclusive evidence for the susceptibility of MXene toward oxidation when stored in ambient conditions (Figure 3f)).[69] Investigations have shown that the oxidation rate of MXene can be slowed either by modifying the solution media,[13,86–88] adding antioxidants[88,89] and polymers,[86] using organic solvents[13,22] or using argon-purged water.[69]

Most recently, through comparison of Ti_3AlC_2 MAX-phase with $Ti_3C_2T_x$ MXene, cubic TiC, and commercially pure Al-1050, XPS investigation identified a redistribution of delocalized electrons from the Ti_3C_2-layers to the Al-layers in Ti_3AlC_2.[74] It was found that the size of this charge redistribution is comparable to the charge rearrangement between Ti atoms and Al atoms in TiAl alloy. This corroboration demonstrates that the laminated layers in the Ti_3AlC_2 are held together through an electrostatic interaction between the slightly positively charged Ti_3C_2-layers and the slightly negatively charged Al-layers. This result shed some light on the mechanism of selective etching in MAX-phase A-layers. If combined with DFT calculations, predicting which MXene compounds can be practically synthesized and estimating the difficulty in removing A-layers in MAX phases would be possible.

Although a powerful technique, XPS has its limitations and disadvantages.[39,46] Foremost, XPS causes the charging of insulating samples, which electrostatically induces peak offsets. As different MXene composites are composed of additives with a range of conductivities at various MXene loading, researchers must be careful when comparing the chemical shifts assigned to certain peaks of interests, as these charging effects often cause position inconsistences.[90] Additionally, approaches toward the curve fitting procedure have been differed across studies and introductions of questionable assumptions, unverified feature assignments, and inconsistent curve fitting have led to contrasting conclusions from XPS analysis.[72] Another notable limitation is the variability of the C 1s position, as it is prone to calibration bias when assigned during data processing. Related to this concern, readers must note that XPS spectra fitting are highly variable as peak assignment is prone to bias, and peak inclusion during analysis can be subjective. Finally, the extreme sensitivity of XPS renders it unable to easily differentiate the effects of impurities from atmosphere and sample defects (e.g., loss of –F and –OH due to exposure to vacuum).[42] Therefore, careful sample preparation, storage, and cleaning (e.g., ion sputtering), as well as experimental controls are required.[42] The above limitations are well recognized when using XPS in MXene research, and further details can be found in other XPS-focused review articles.[39,46]

2.2.2. In Situ X-Ray Absorption Spectroscopy

XAS is a versatile tool for studying the fundamental electronic states of materials. When incident X-ray photons hit a sample, a sharp increase in absorption energy called an absorption edge is observed. This sharp increase corresponds to the energy required to eject a core electron to the lowest unoccupied molecular orbital or to the continuum, producing a photoelectron, referred to as either K-edge (1s electron) or L-edge (2s or 2p electron) absorption. The XAS region (**Figure 4**a) can be divided into X-ray absorption near-edge structure (XANES) and extended X-ray absorption fine structure (EXAFS), which respectively provide information on oxidation state, bond length, and coordination number.[41,43,91,92]

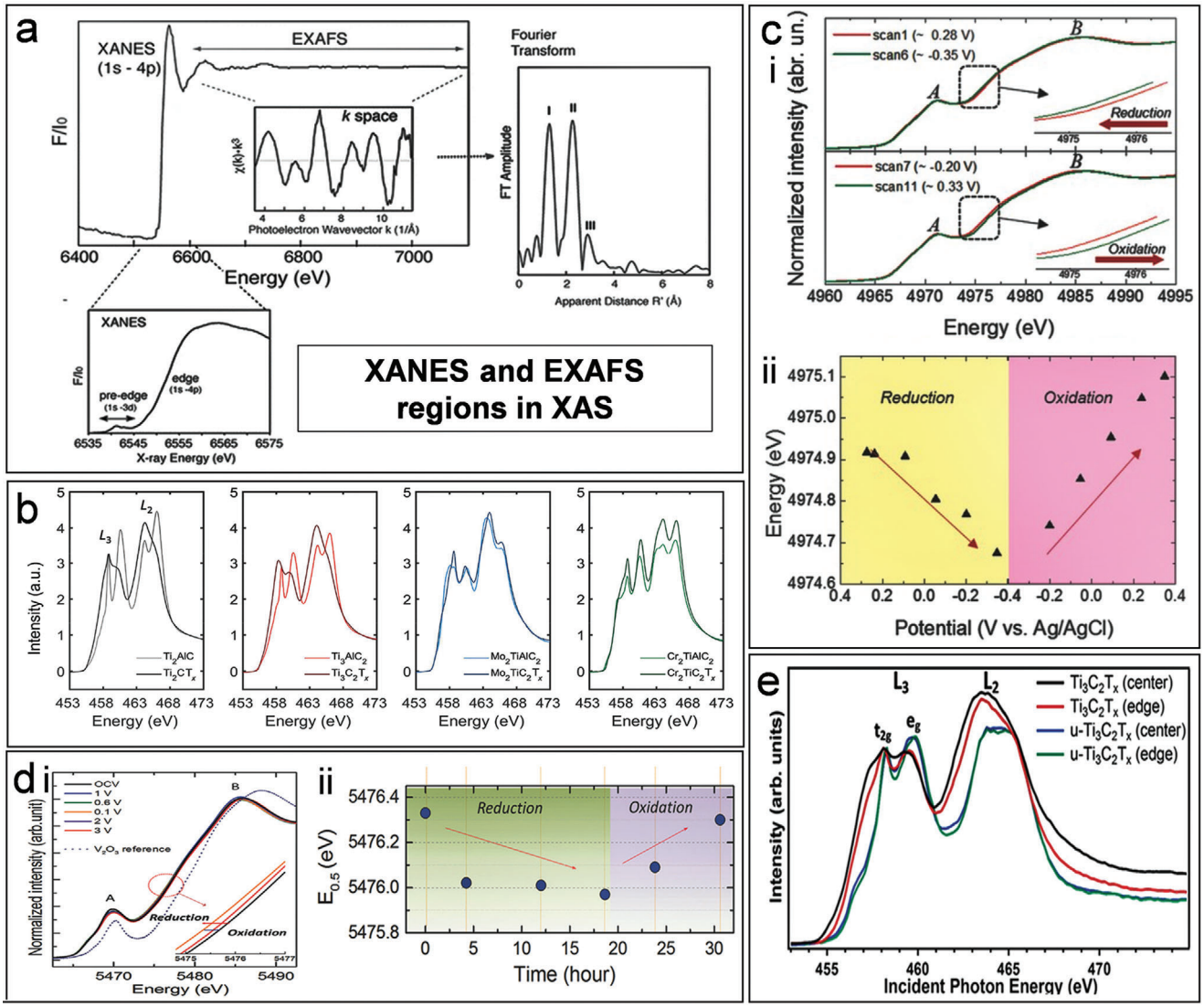

Figure 4. a) A K-edge XAS spectra, showing the combined XANES and EXAFS regions. Enlarged sections show the K-edge XANES, k-space EXAFS spectrum, and a Fourier transform of the k-space EXAFS data. Reproduced with permission.[91] Copyright 2022, Springer Nature Switzerland AG. b) XAS measurements of (1) Ti_2CT_x and Ti_2AlC, (2) $Ti_3C_2T_x$ and Ti_3AlC_2, (3) $Mo_2TiC_2T_x$ and Mo_2TiAlC_2, and (4) $Cr_2TiC_2T_x$ and Cr_2TiAlC_2 at the Ti $L_{2,3}$-edge. Reproduced with permission.[48] Copyright 2022, IOP Publishing. c) (i) Ti K-edge XANES spectra of $Ti_3C_2T_x$, collected at 0.3 to −0.35 V and −0.2 to 0.35 V (vs Ag/AgCl), (ii) a plot of the Ti edge energy against potential across a full electrochemical cycle. Reproduced with permission.[49] Copyright 2015, Wiley-VCH GmbH. d) (i) V K-edge XANES spectra of V_2CT_x during ex situ Na^+ intercalation/deintercalation process from OCV to 3 V, showing (ii) how V edge energy varied with cell voltage. Reproduced with permission.[50] Copyright 2017, Wiley-VCH GmbH. e) (i) Ti L-edge XA spectra of single flakes of pristine $Ti_3C_2T_x$ and u-$Ti_3C_2T_x$. Reproduced with permission.[93] Copyright 2020, American Chemical Society.

XAS-based techniques have been used to identify the fundamental electronic states of MXenes, specifically the oxidation states of their transition metal components. For example, XAS showed that the oxidation state of the Ti atoms varies depending on the number of transition metal layers.[48] In Ti_2CT_x, all Ti atoms are attached to surface terminations, resulting in significantly higher Ti $L_{2,3}$-edge spectra upon conversion from Ti_2AlC MAX to MXene, while $Ti_3C_2T_x$ has one Ti layer within its backbone protected by adjacent C atoms (Figure 4b). This has been identified as the reason why Ti_2CT_x is more susceptible to oxidation compared to $Ti_3C_2T_x$. It was also found that in ordered double transition metal MXenes, the outer layer (whether $Mo_2TiC_2T_x$ or $Cr_2TiC_2T_x$) acts as sacrificial layer, inhibiting the oxidation of the inner Ti layer.[48]

A major advantage of XAS over conventional X-ray-based spectroscopic techniques like XPS is its capability to describe how the transition metal oxidation state changes in situ during chemical and electrochemical processes. For instance, Lukatskaya et al.[49] monitored the XANES spectra of $Ti_3C_2T_x$ during charging–discharging cycling in acidic electrolyte (Figure 4c(i)). By analyzing the energies acquired (Figure 4c(ii)), the average oxidation state of Ti was shown to change from 2.33 to 2.43 (i.e., by 0.1 ē per Ti atom) over a 0.7 V window, suggesting a redox energy storage mechanism for the system.[49] This technique has also been used

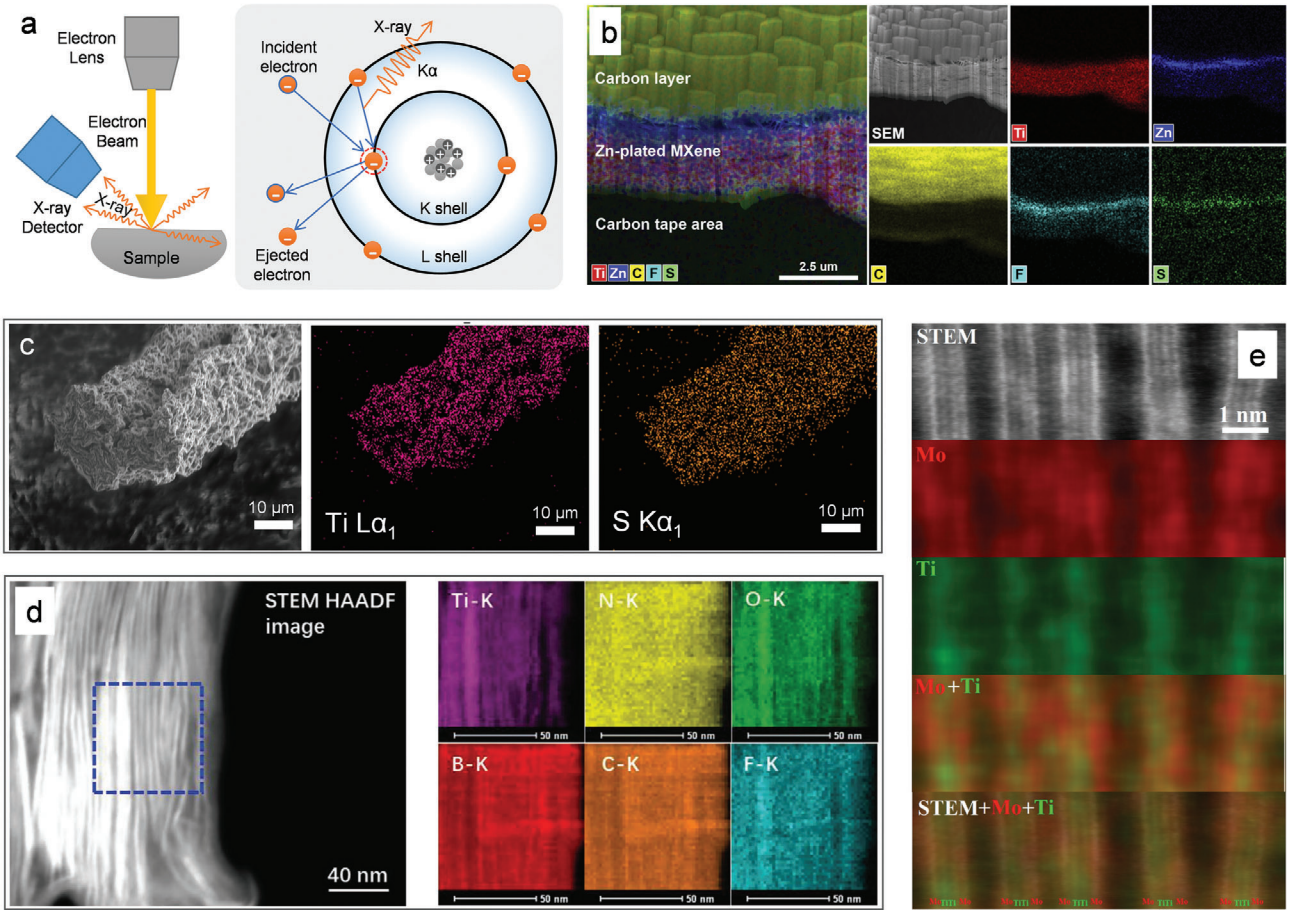

Figure 5. a) The main components of EDX spectroscopy and a scheme of associated X-ray generation. b) Spatially resolved elemental EDX maps of a representative MXene@Zn paper cross-section. The left-hand side panel shows an overlay of all five elemental maps. The terraced shapes above MXene come from the carbon-coating used to prepare the cross-section and $Zn(CF_3SO_3)_2$ electrolyte is the source of the F and S signals. Reproduced with permission.[96] Copyright 2020, Elsevier Ltd. c) SEM images of the cross-section of a typical PEDOT:PSS/MXene fiber and EDX elemental maps of titanium and sulphur of the sample. Reproduced with permission.[33] Copyright 2019, Wiley-VCH GmbH. d) STEM HAADF image and EDX mapping of MXene–borate–PEI cross-linked at 75 °C (MBP-75). The blue dashed box indicates the area chosen for EDX mapping. Reproduced with permission.[104] Copyright 2018, Wiley-VCH. e) HRSTEM of $Mo_2Ti_2C_3$ along the [11 2 0] zone axis, EDX mapping on e) for Mo, Ti, and their overlays showing the Mo atoms in red, Ti atoms in green. Reproduced with permission.[106] Copyright 2015, American Chemical Society.

to probe vanadium oxidation state changes in V_2CT_x (≈0.4 eV) during cycling of Na-ion batteries in operando (Figure 4d).[50] A study by Al-Temimy et al.[93] demonstrated that XAS can be used to determine Ti oxidation state changes in MXene upon intercalation of molecules such as urea (referred to as u-$Ti_3C_2T_x$). Most Ti atoms exhibited oxidation state close to Ti^{4+} after urea intercalation compared to the pristine $Ti_3C_2T_x$ (Figure 4e).[93] Interestingly, the spatial resolution of this method gave higher Ti oxidation state at the edge than on the basal plane. Despite the growing interest in XAS, this technique has yet to achieve similar popularity as XPS or XRD, as it generally requires synchrotron radiation to generate the required X-ray brightness.[41] Bench-top systems have recently become available, but their capabilities remain limited.[94]

2.2.3. Energy-Dispersive X-Ray (EDX or EDS) Analysis

Besides directly using X-rays as the energy source, they can also be generated when a material surface is exposed to high energy electron beams, like how they are emitted in X-ray tubes. One technique utilizing such X-ray generation mechanisms is energy-dispersive X-ray spectroscopy (EDX or EDS), which is a widely used characterization method typically coupled with SEM. In EDX, an electron beam hitting an atom's inner shell knocks an activated electron out of its original orbital, leaving behind a positively charged electron hole. The electron hole attracts another electron to fill the vacancy, which releases X-rays when this electron moves from an outer higher-energy orbital to this inner lower-energy orbital (**Figure 5**a).[95] The energy of these X-rays is unique to every element and can be used for both qualitative and quantitative analysis, enabling identification of both elemental type and proportion in a sample.

EDX is commonly used for mapping MXene distribution in composite systems. For instance, Zn deposition on MXene paper for subsequent electrochemical studies was confirmed using spatially resolved EDX mapping of Zn-plated Ti_3C_2 electrode cross-sections.[96] The elemental maps show sufficient Zn coverage, with a somewhat higher Zn concentration on the planar surface

furthest from the nylon separator (Figure 5b). For this analysis, it should be emphasized that components of a hybrid or composite sample must possess distinguishable elements to accurately describe their distribution. For example, in MXene/PEDOT:PSS composite fibers, the MXene is the only Ti source, while S only comes from PEDOT:PSS. A comparison of the Ti and S distributions indicated uniform infiltration of PEDOT:PSS between MXene layers (Figure 5c).[33] By contrast, the presence of carbon and oxygen in both MXene and graphene oxide/reduced graphene oxide leads to inaccurate information on the distribution of MXenes in the EDX elemental map of MXene/graphene hybrid fibers.[97] However, EDX has some limitations in precisely evaluating the amount of all elements in MXene and their composites, particularly when light elements such as O or F are present in the terminal groups.[98] Also, EDX studies have difficulty in distinguishing impurities from atmosphere or during sample synthesis.[99–101]

EDX analysis can also be used alongside TEM to achieve high resolution and local elemental information.[102,103] For example, Shen et al.[104] applied the high-angle annular dark field (HAADF) scanning transmission electron microscopy (STEM) and the associated EDX elemental mapping to study the microstructure of functionalized MXene layers at a 40 nm scale. MXene lattice fringes can be clearly observed, indicating the ordered stacking structure. The uniform distribution of the elements Ti, B, N, C, O, and F suggests the successful interlocking of MXene nanofilm with borate and PEI molecules (Figure 5d).[104] Tandem STEM and XRD enables direct identification of the crystal structure paralleled with determination of the spatial distribution of the elements in the lattice. As an example, Anasori et al.[105] used EDX mapping to prove the atomic-scale formation of the out-of-plane ordered Mo_2TiAlC_2 o-MAX phase and its corresponding Mo_2TiC_2 o-MXene. Another work presented HRSTEM images of $Mo_2TiC_2T_x$ after Al etching, with the atomic ordering of Ti (green) sandwiched between two Mo layers (red) confirmed by EDX mapping (Figure 5e).[106] This work confirmed a new double transition metal carbide $M'_2M''_2C_3$, where M′ and M″ are two different early transition metals, Ti and Mo.

2.3. Structural Analysis of Different Scale Syntagms

2.3.1. Microcomputed Tomography (Micro-CT)

Micro-CT, also called microtomography or microcomputed tomography, is an emerging 3D imaging technique that utilizes X-rays to examine cross-sections of an object at pixel sizes as small as 100 nm. Compared with single layer graphene or polymers, MXene has high contrast under X-rays, a characteristic that can be exploited using micro-CT to study the MXene distribution in composites. Micro-CT can also be performed without sample post-treatment, so the integrity of the structural character is retained.[107] To the best of our knowledge, the first application of micro-CT in visualizing a MXene microstructure was carried out in 2018 using $Ti_3C_2T_x$ MXene/cellulose aerogel composites,[108] which showed evenly distributed lamellar channels throughout the monolithic sample, formed during the freezing process (**Figure 6**a). The reconstructed images from micro-CT scans easily illustrated the porosity of the aerogel samples, allowing further investigation on the structural evolution of the samples. Rozmyslowska-Wojciechowska et al.[109] found that adding $Ti_3C_2T_x$ MXene flakes into porous chitosan–hyaluronate aerogels causes a decrease in the porosity and height of the composite. In another case, micro-CT measurements have also identified defects in other MXene structures at various resolutions. When building the electrothermal heaters of epoxy resin/$Ti_3C_2T_x$ MXene composites, where the MXene serves as a nanoheater and the epoxy resin spreads the heat, micro-CT showed that no unfilled pores were visible within the volume, confirming the infiltration of epoxy throughout the aerogel structure.[110] Besides applications in materials science, the micro-CT technique also contributed to understanding how MXene can be used in biomedical applications, specifically in bone regeneration.[111–113] Micro-CT aids in visualizing good biocompatibility, osteoinductivity, and bone regeneration activity of MXene-based structures in vivo.[107,114,115]

Micro-CT is also important for understanding the influence of different manufacturing methods or procedures on the porosity and structural defects in MXene-based structures. The comparison of micro-CT images of MXene/cellulose nanofiber films produced by blade-coating and by drop-casting showed that the blade-coated film exhibits a smooth compact structure with low porosity (≈6.9%, Figure 6b).[116] By contrast, the porosity of drop-cast film dramatically increased to ≈29.0%, with the film possessing a loose structure and craggy surface. To further decrease the porosity and defects in MXene films, Cheng's group used sequential bridging with hydrogen and covalent bonding agents, which resulted in highly densified MXene films.[51] Nano-CT, a higher resolution micro-CT that uses a similar graphing mechanism, was adopted to confirm the relative absence of small voids in densified samples. Moreover, comparing 3D void microstructures of the samples obtained using focused ion beam scanning electron microscope tomography (FIB/SEMT) and nano-CT showed that the latter provides higher resolution imaging (Figure 6c,d). Still, extremely small voids with voxel sizes of tens of nanometers cannot be observed by nano-CT or FIB/SEMT. Thus, the porosities derived from the corresponding 3D reconstructions are lower than those derived from density measurements.[51]

Due to its contactless nature, samples can be studied during mechanical deformation, thereby allowing micro-CT to monitor dynamic structural evolution and to be used for precise engineering of microstructures. Micro-CT images of MXene aerogel taken at various compressive strains reveal that lamellae walls can crumble with microstructural changes. This results in a substantial change in the microstructure, potentially closing and/or blocking the openings within the walls as the walls get closer (Figure 6e).[117] Rawson et al.[118] classified the orientation of lamellar channels in MXene aerogels according to the polar angle of their sheet relative to the loading direction (Z) in 10° increments (Figure 6f). By an in situ micro-CT compression tests, they found that the predominant intradomain behavior is sheet reorientation toward the loading direction (Z) and simultaneous reduction in sheet spacing (Figure 6g). The sheets initially aligned parallel with the loading direction ($\varphi \approx 80°–90°$), which largely maintain their alignment and their sheet spacing.

Recently, micro-CT also demonstrated advantages in characterizing solvent-rich anhydrous gel containing large amounts of glycerol, making SEM microstructural observations impractical.

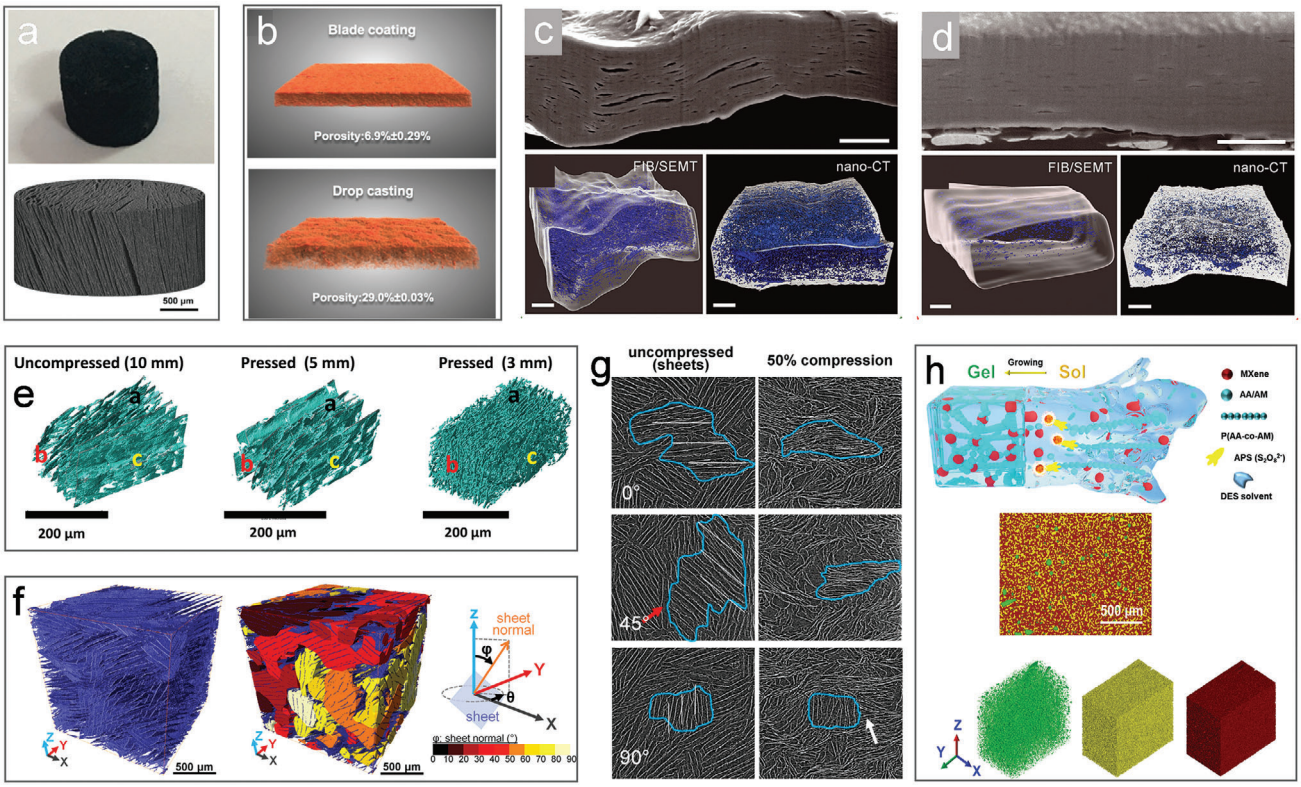

Figure 6. a) Digital photographs of the $Ti_3C_2T_x$ MXene/cellulose aerogel and its micro-CT image. Reproduced with permission.[108] Copyright 2018, Royal Society of Chemistry. b) 3D reconstruction of the cross-section derived from micro-CT for MXene/cellulose nanofiber films prepared by blade-coating and drop-casting. Reproduced with permission.[116] Copyright 2022, American Chemical Society. SEM images of MXene film cross-sections c) without and d) with sequential bridging cut by an FIB and the 3D-reconstructed void microstructure derived from FIB/SEMT for MXene. Reproduced with permission.[51] Copyright 2021, American Association for the Advancement of Science. e) MXene aerogel scanned with micro-CT at three different stages: uncompressed (initial thickness 10 mm), compressed to 5 mm, and compressed to 3 mm. f) The original 3D reconstruction of the aerogel sheets and the domains colored with orientations segmented (in 10° bins from dark red to pale yellow) according to their sheet normal orientation alongside the aerogel sheets. Reproduced with permission.[118] Copyright 2022, American Chemical Society. g) Subvolumes of the CT data of MXene aerogels at uncompressed and 50% of compression, showing sheet spacing reduction for initially 0° orientation, while sheet spacing reduction and rotation for initially 45° orientation and the buckling structure at initially 90° orientation. Reproduced with permission.[117] Copyright 2019, American Chemical Society. h) Microscopic 3D structure and composition of MXene-based hydrogel, green represents air or bubbles, yellow represents solvent, red represents MXene cross-linked polymer (note: density (ρ) increases from left to right). Reproduced with permission.[119] Copyright 2022, Elsevier Ltd.

By applying micro-CT, one can easily recognize the individual components, such as the microbubbles (green) generated by the polymerization exotherm evenly distributed in the gel, and the lower density solvent (yellow) filled with the high density MXene–polymer network (red) (Figure 6h).[119] However, it remains a big challenge of analyzing low contrast samples for micro-CT due to scarce X-ray attenuation features, particularly for sponges and foam-like structures.[120,121] This limitation can be overcome to some extent by adjusting the working parameters of micro-CT equipment. However, such approach also facilitates noise and artefacts, and solving the signal-to-noise trade-off has always been a challenge. Since the application of micro-CT in MXenes is relatively new, those technical issues have not yet been discussed.

2.3.2. Small-/Wide-Angle X-Ray Scattering (SAXS/WAXS)

SAXS is a technique that records scattered X-rays, typically measured at small angles (0.1°–10°) after an incident beam illuminates a sample. This analysis can determine nanoparticle size distributions,[122] resolve the size and shape of (monodisperse) macromolecules,[122,123] measure pore sizes[123] and characteristic distances of partially ordered materials,[124] and much more. Similarly, WAXS measures scattered X-rays, but at larger angles (>10°), thus requiring a much shorter sample-to-detector distance when acquiring crystallographic information (**Figure 7**a). In most SAXS instruments, this sample-to-detector distance can be adjusted so that diffractometers can also perform WAXS in a single run. Generally, the 2D scattering patterns generated from SAXS/WAXS experiments provide information through a series of data reductions (i.e., extracting plots from diffractograms, followed by integration of a target data), of either the radial (q_x and q_y) and/or azimuthal directions (ϕ) of the signals. Integrating the scattering intensity along the radial direction extracts information about the void and crystallite dimensions, regardless of orientation.[15] Meanwhile, integrating the scattering intensity along the azimuthal direction allows us to determine the preferential alignment of such voids and crystallites. The utilization

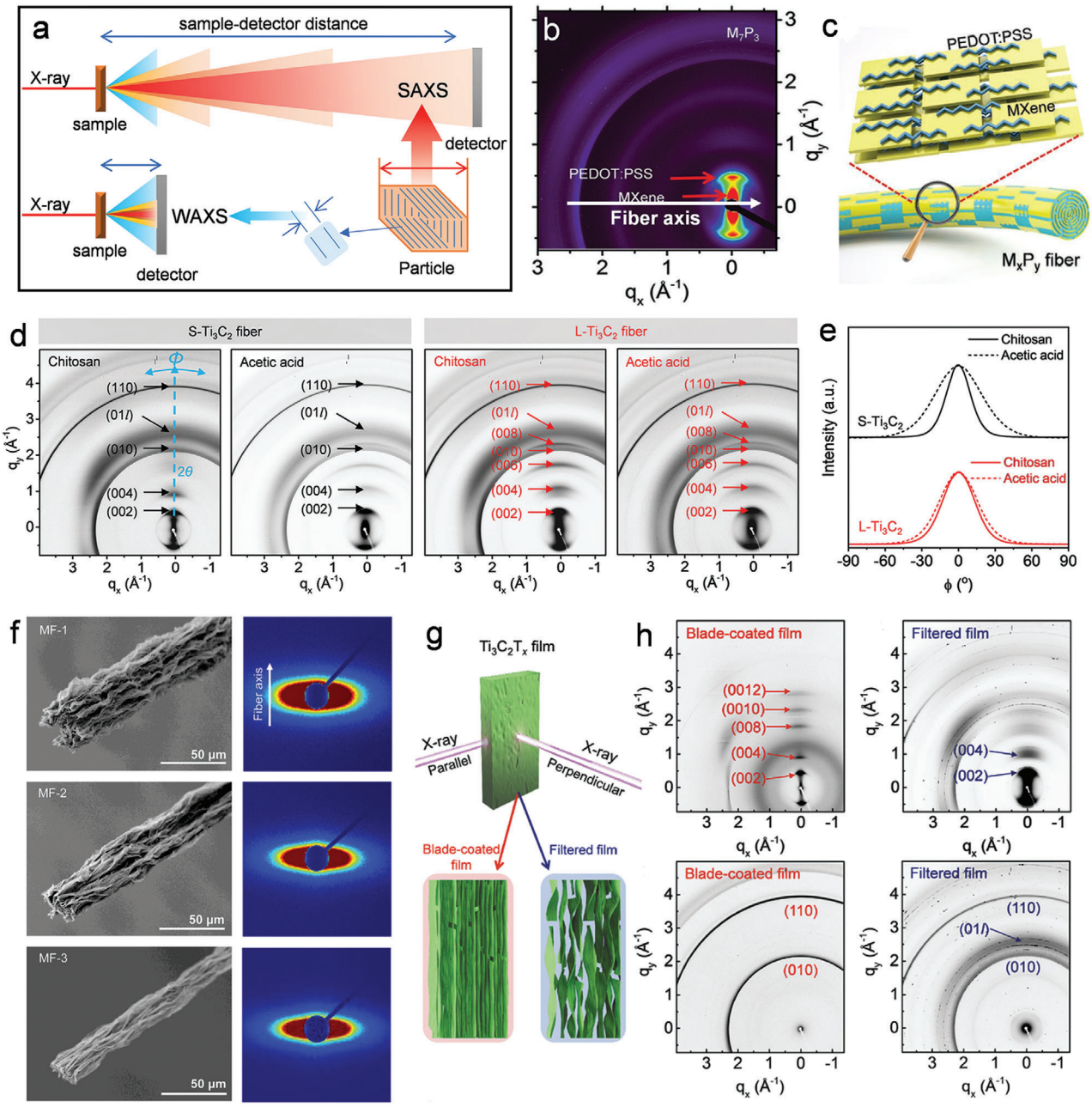

Figure 7. a) Illustration of an instrumental configuration of SAXS/WAXS measurement. b) 2D SAXS/WAXS images of PEDOT:PSS/MXene fiber. c) Schematic illustration of the alignment of MXene flakes and PEDOT:PSS chains inside composite fibers. (b,c) Reproduced with permission.[33] Copyright 2019, Wiley-VCH GmbH. d) SAXS/WAXS scattering patterns of small MXene (S-Ti_3C_2) and large MXene (L-Ti_3C_2) fibers spun in chitosan and acetic acid baths. e) Azimuthal plot of scattering at (002) along the azimuthal direction in the region of ±90°. Reproduced with permission.[15] Copyright 2020, American Chemical Society. f) SEM image and SAXS patterns of MXene fibers stretched at different ratios. Reproduced with permission.[126] Copyright 2021, American Chemical Society. g) Schematic illustration of the positions of the X-ray beam (parallel and perpendicular to the MXene film plane) in SAXS/WAXS measurement. The bottom shows the predicated microstructure and orientation of MXene flakes within films produced by blade-coating and vacuum-assisted filtration. h) SAXS/WAXS patterns of MXene films when the film plane is (top) parallel and (bottom) perpendicular to the X-ray beam. Reproduced with permission.[31] Copyright 2020, Wiley-VCH GmbH.

of SAXS/WAXS on MXene-based materials was first reported by Zhang et al.,[33] who explored the stacking and alignment of MXene flakes in poly(3,4-ethylenedioxythiophene):polystyrene sulfonate (PEDOT:PSS)/MXene fibers. Here, fiber samples mounted horizontally with respect to the beam produced X-ray scattering signals toward the vertical (meridian) and horizontal (equatorial) directions, representing MXene sheets oriented parallel and perpendicular to the fiber axis, respectively (Figure 7b). The orientation of PEDOT:PSS chains and MXene flakes relative to the fiber axis was quantified by the Herman's orientation factor

(f), which can be estimated by fitting the (002) scattering intensity along the azimuthal direction (ϕ). In this analysis, f values ranging from 0 to 1 imply random flake orientation to complete alignment, respectively. Zhang et al.[33] demonstrated that in a PEDOT:PSS/MXene fiber, the PEDOT:PSS chains ($f = 0.74$) have an almost identical f value to MXene flakes ($f = 0.73$), suggesting good alignment of both materials along the fiber axis (Figure 7c). This study also confirmed that a synchrotron-based X-ray source enables quicker collection of 2D scattering patterns from a single filament and provides more accurate structural information than testing a bundle of filaments.

SAXS/WAXS measurements may also detect the structural changes within a fiber interior caused by variations in the critical parameters of material fabrication (e.g., wet spinning).[15,125] For example, Zhang et al.[15] compared the SAXS/WAXS patterns of MXene fibers produced using two MXene sheet sizes coagulated at different rates (Figure 7d). Calculating the f values from the (002) azimuthal (ϕ) plots in Figure 7e revealed that MXene fibers spun in the chitosan bath ($f = 0.83$) have greater anisotropic arrangement than those spun in acetic acid ($f = 0.58$). These results indicate that slow coagulation in chitosan promoted better alignment of MXene flakes, compared to the faster coagulation rates in acetic acid. Finally, SAXS/WAXS has also verified that large MXene flakes tend to be more aligned than small flakes.[15] Another study utilized the azimuthal patterns of SAXS signal to quantify the orientation of microvoids in MXene fibers (Figure 7g) by calculating the orientation angle (Bg) via the Ruland Streak method.[126] It was found that the radian Bg of MXene fibers spun with increasing draw ratios decreased from 0.66 to 0.51, demonstrating that parallel alignment of microvoids to the fiber axis increases upon application of strong external shear forces.[126]

Aside from fibers, SAXS/WAXS measurements are also applicable to high performance MXene films.[28,31,45,116,127] Zhou et al.[128] found through SAXS/WAXS that graphene/MXene composite films possess better alignment than pure graphene film. However, unlike 1D fiber samples, 2D MXene-based films exhibit variable SAXS/WAXS patterns. In particular, the scattering profile of films varies with sample orientation relative to the incident X-rays.[31,45,129] This was shown through the work of Zhang et al.,[31] where MXene films oriented parallel to the X-ray beam exhibit scattering patterns (along q_y) assigned to (002), (004), and (008) peaks (Figure 7h top), evidence of highly aligned flake orientations along the film plane. By contrast, patterns obtained from samples mounted perpendicular to the beam only showed the (010) and (110) planes of the *P63/mmc* unit cells of $Ti_3C_2T_x$ for the blade-coated film, which cannot be observed in the parallel test configuration (Figure 7h bottom) or if the MXene sample is in a fiber format (Figure 7d). The clean patterns indicate that the $P6_3/mmc$ unit cells lie perfectly parallel to the film plane with minimum disorientation. On the other hand, MXene flakes stack in a wrinkled manner when filtered. The intensity of the (010) and (110) peaks significantly decreased, and several (01l) scattering peaks attributed to (011), (013), (014), and (016) planes were evident for the filtered film, indicating that the $P6_3/mmc$ unit cells are oriented at an angle relative to the film plane.[31] These observations suggest that sample orientation is of great importance to the conduct of SAXS/WAXS experiments, especially when analyzing 2D nanomaterial-based samples. The structural changes in MXene-based films require collection of SAXS/WAXS patterns in both parallel and perpendicular directions, as demonstrated through follow-up studies using sequentially bridged MXene[45] and MXene/cellulose nanocrystal films.[28]

3. Summary and Outlook

As MXene research expands and advances toward practicality, it is imperative to study the fundamental properties of MXenes and their behavior in varying conditions to establish proper correlations among structure, chemistry, and performance. The increasing availability of intense X-ray sources, high-speed detectors, and faster methods of analyzing data allow researchers to examine these 2D structures at high spatial resolution and small timescale.[26,102] This review explored how X-rays can be utilized to perform MXene analysis in ways that complement other techniques, whether they are also X-ray based or not. Among them, XRD, the most basic and accessible among these techniques, remains the common characterization technique used across MXene research. Meanwhile, indispensable spectroscopic X-ray techniques, such as XPS, XAS, and EDS, provide information on chemical properties, enabling understanding of performance and translation to a wide variety of applications (e.g., supercapacitors). XPS is a quantitative tool for assessing elemental profile, sensitive surface chemistry, and chemical stability, and has been vital from MXene discovery in 2011 to recent developments in composites research. XAS-based techniques have been used as a more sensitive approach to quantitatively identify transition metal oxidation states, allowing the analyses of electronic properties and in situ electrochemical processes. On the other hand, EDS serves as a rapid tool to confirm the presence of atoms of interest in both MXene and its composites, despite providing less information than XPS and XAS. Besides the traditional use of these techniques, the in situ and in operando measurements of these techniques have getting more popular, which enable the understanding of how the structure and chemistry change during chemical or physical procedures of MXenes.

Whilst much of this article detailed the most widely used X-ray techniques for MXenes, it also highlighted other specialized techniques that can probe certain properties or structures. For instance, the structural insight micro-CT provides has advanced the understanding of mechanisms governing MXene architecture assembly, which requires fast scanning and high-resolution imaging methods.[101] Likewise, the recent developments in SAXS and WAXS have provided structural information that otherwise cannot be acquired through traditional XRD methods. While X-ray-based techniques are indeed becoming more popular, it is expected that high intensity sources at large synchrotron-scale facilities will remain the primary option for most (if not all) cutting-edge SAXS/WAXS experiments, especially since these techniques also enable analysis of small samples and rapid in situ experiments. More accessible measurements like the use of variable wavelengths for anomalous scattering experiments or the use of lab-scale X-ray sources may be explored in the future, although the data quality maybe inferior to that obtained using synchrotron facilities.

Maximizing the use of X-ray-based techniques can lead to new discoveries that have enduring positive impacts on the synthesis, functionalization, and processing of MXenes. For instance, as solution-based processing of MXenes is becoming the preferred

route toward functional architectures, we also predict that the current X-ray techniques will evolve for the feasibility of liquid sample analysis. This evolution is expected to improve our understanding of MXene self-assembly, including how sheet orientation changes in dispersions and the parameters/factors that influence such processes. In addition, the complex chemistry and structure of MXenes demands the use of additional mathematical and chemical simulations to aid in providing more valid interpretations of experimental data acquired through X-ray-based methods. For example, structural modeling and computational analysis in tandem with XPS data to show structure and defects of MXenes can provide deeper insights into their mechanical stability, chemical reactivity, and electrical/electrochemical properties. Likewise, mathematical modeling and machine learning techniques to aid the typically exhaustive SAXS/WAXS data processing would enable quicker acquisition and improved interpretation of the microstructural parameters of MXene-based architectures. We envisage that the knowledge gained from this exciting new frontier may also be adapted to a larger family of 2D nanomaterials, paving the way for their potential widespread utilization in practical applications.

Acknowledgements

The authors acknowledge the financial support from the Australian Research Council (FT130100380 and IH210100023), and the Australian National Fabrication Facility (ANFF) Victorian node at Deakin University. The authors also acknowledge the provision of experimental beamtime on the SAXS–WAXS beamline at the Australian Synchrotron (part of ANSTO) and the Deakin-CSIRO InSitX X-ray facility.

Open access publishing facilitated by Deakin University, as part of the Wiley - Deakin University agreement via the Council of Australian University Librarians.

Conflict of Interest

The authors declare no conflict of interest.

Keywords

micro-CT, MXenes, SAXS/WAXS, X-rays, XRD

Received: November 20, 2022
Revised: January 19, 2023
Published online:

[1] A. Shayesteh Zeraati, S. A. Mirkhani, P. Sun, M. Naguib, P. V. Braun, U. Sundararaj, *Nanoscale* **2021**, *13*, 3572.
[2] T. S. Mathis, K. Maleski, A. Goad, A. Sarycheva, M. Anayee, A. C. Foucher, K. Hantanasirisakul, C. E. Shuck, E. A. Stach, Y. Gogotsi, *ACS Nano* **2021**, *15*, 6420.
[3] M. Boota, B. Anasori, C. Voigt, M.-Q. Zhao, W. Barsoum Michel, Y. Gogotsi, *Adv. Mater.* **2015**, *28*, 1517.
[4] J. Zhang, S. Seyedin, Z. Gu, W. Yang, X. Wang, J. M. Razal, *Nanoscale* **2017**, *9*, 18604.
[5] M. Ghidiu, M. R. Lukatskaya, M.-Q. Zhao, Y. Gogotsi, M. W. Barsoum, *Nature* **2014**, *516*, 78.
[6] X. Wang, S. Kajiyama, H. Iinuma, E. Hosono, S. Oro, I. Moriguchi, M. Okubo, A. Yamada, *Nat. Commun.* **2015**, *6*, 6544.
[7] J. Halim, M. R. Lukatskaya, K. M. Cook, J. Lu, C. R. Smith, L.-Å. Näslund, S. J. May, L. Hultman, Y. Gogotsi, P. Eklund, M. W. Barsoum, *Chem. Mater.* **2014**, *26*, 2374.
[8] A. D. Dillon, M. J. Ghidiu, A. L. Krick, J. Griggs, S. J. May, Y. Gogotsi, M. W. Barsoum, A. T. Fafarman, *Adv. Funct. Mater.* **2016**, *26*, 4162.
[9] M. Mariano, O. Mashtalir, F. Q. Antonio, W.-H. Ryu, B. Deng, F. Xia, Y. Gogotsi, A. D. Taylor, *Nanoscale* **2016**, *8*, 16371.
[10] A. Ali, A. Belaidi, S. Ali, M. I. Helal, K. A. Mahmoud, *J. Mater. Sci.* **2016**, *27*, 5440.
[11] B. Xu, M. Zhu, W. Zhang, X. Zhen, Z. Pei, Q. Xue, C. Zhi, P. Shi, *Adv. Mater.* **2016**, *28*, 3333.
[12] J. Liu, H.-B. Zhang, R. Sun, Y. Liu, Z. Liu, A. Zhou, Z.-Z. Yu, *Adv. Mater.* **2017**, *29*, 1702367.
[13] K. Maleski, V. N. Mochalin, Y. Gogotsi, *Chem. Mater.* **2017**, *29*, 1632.
[14] B. Akuzum, K. Maleski, B. Anasori, P. Lelyukh, N. J. Alvarez, E. C. Kumbur, Y. Gogotsi, *ACS Nano* **2018**, *12*, 2685.
[15] J. Zhang, S. Uzun, S. Seyedin, P. A. Lynch, B. Akuzum, Z. Wang, S. Qin, M. Alhabeb, C. E. Shuck, W. Lei, E. C. Kumbur, W. Yang, X. Wang, G. Dion, J. M. Razal, Y. Gogotsi, *ACS Cent. Sci.* **2020**, *6*, 254.
[16] S. Seyedin, J. Zhang, K. A. S. Usman, S. Qin, A. M. Glushenkov, E. R. S. Yanza, R. T. Jones, J. M. Razal, *Global Chall.* **2019**, *3*, 1900037.
[17] Q. Zhang, H. Lai, R. Fan, P. Ji, X. Fu, H. Li, *ACS Nano* **2021**, *15*, 5249.
[18] R. Bian, G. He, W. Zhi, S. Xiang, T. Wang, D. Cai, *J. Mater. Chem. C* **2019**, *7*, 474.
[19] M. Naguib, O. Mashtalir, J. Carle, V. Presser, J. Lu, L. Hultman, Y. Gogotsi, M. W. Barsoum, *ACS Nano* **2012**, *6*, 1322.
[20] A. Lipatov, M. Alhabeb, M. R. Lukatskaya, A. Boson, Y. Gogotsi, A. Sinitskii, *Adv. Electron. Mater.* **2016**, *2*, 1600255.
[21] M. Alhabeb, K. Maleski, B. Anasori, P. Lelyukh, L. Clark, S. Sin, Y. Gogotsi, *Chem. Mater.* **2017**, *29*, 7633.
[22] S. Seyedin, E. R. S. Yanza, Joselito M. Razal, *J. Mater. Chem. A* **2017**, *5*, 24076.
[23] M. Naguib, M. Kurtoglu, V. Presser, J. Lu, J. Niu, M. Heon, L. Hultman, Y. Gogotsi, W. Barsoum Michel, *Adv. Mater.* **2011**, *23*, 4248.
[24] T. Bilyk, M. Benchakar, M. Bugnet, L. Loupias, P. Chartier, H. Pazniak, M. L. David, A. Habrioux, S. Celerier, J. Pacaud, V. Mauchamp, *J. Phys. Chem. C* **2020**, *124*, 27071.
[25] J. L. Hart, K. Hantanasirisakul, A. C. Lang, Y. Li, F. Mehmood, R. Pachter, A. I. Frenkel, Y. Gogotsi, M. L. Taheri, *Adv. Mater. Interfaces* **2021**, *8*, 2001789.
[26] J. Palisaitis, I. Persson, J. Halim, J. Rosen, P. O. Å. Persson, *Nanoscale* **2018**, *10*, 10850.
[27] H. Jing, H. Yeo, B. Lyu, J. Ryou, S. Choi, J.-H. Park, B. H. Lee, Y.-H. Kim, S. Lee, *ACS Nano* **2021**, *15*, 1388.
[28] K. A. S. Usman, C. J. O. Bacal, J. Zhang, S. Qin, P. A. Lynch, P. Mota-Santiago, M. Naebe, L. C. Henderson, D. Y. Hegh, J. M. Razal, *Macromol. Rapid Commun.* **2022**, *43*, 2200114.
[29] K. A. S. Usman, S. Qin, L. C. Henderson, J. Zhang, D. Y. Hegh, J. M. Razal, *Mater. Horiz.* **2021**, *8*, 2886.
[30] K. A. S. Usman, J. Zhang, C. J. O. Bacal, S. Qin, P. Mota-Santiago, P. A. Lynch, M. Naebe, L. C. Henderson, D. Hegh, J. M. Razal, *2D Mater.* **2022**, *9*, 044003.
[31] J. Zhang, N. Kong, S. Uzun, A. Levitt, S. Seyedin, P. A. Lynch, S. Qin, M. Han, W. Yang, J. Liu, X. Wang, Y. Gogotsi, J. M. Razal, *Adv. Mater.* **2020**, *32*, 2001093.
[32] Z. Ling, C. E. Ren, M.-Q. Zhao, J. Yang, J. M. Giammarco, J. Qiu, M. W. Barsoum, Y. Gogotsi, *Proc. Natl. Acad. Sci. USA* **2014**, *111*, 16676.
[33] J. Zhang, S. Seyedin, S. Qin, Z. Wang, S. Moradi, F. Yang, P. A. Lynch, W. Yang, J. Liu, X. Wang, J. M. Razal, *Small* **2019**, *15*, 1804732.
[34] X. Shi, H. Wang, X. Xie, Q. Xue, J. Zhang, S. Kang, C. Wang, J. Liang, Y. Chen, *ACS Nano* **2019**, *13*, 649.
[35] Y. Yue, N. Liu, Y. Ma, S. Wang, W. Liu, C. Luo, H. Zhang, F. Cheng, J. Rao, X. Hu, J. Su, Y. Gao, *ACS Nano* **2018**, *12*, 4224.
[36] E. A. Mayerberger, O. Urbanek, R. M. McDaniel, R. M. Street, M. W. Barsoum, C. L. Schauer, *J. Appl. Polym. Sci.* **2017**, *134*, 45295.

[37] J. L. Hart, K. Hantanasirisakul, A. C. Lang, B. Anasori, D. Pinto, Y. Pivak, J. T. van Omme, S. J. May, Y. Gogotsi, M. L. Taheri, *Nat. Commun.* **2019**, *10*, 522.
[38] M. Naguib, T. Saito, S. Lai, M. S. Rager, T. Aytug, M. Parans Paranthaman, M.-Q. Zhao, Y. Gogotsi, *RSC Adv.* **2016**, *6*, 72069.
[39] M. Shekhirev, C. E. Shuck, A. Sarycheva, Y. Gogotsi, *Prog. Mater. Sci.* **2021**, *120*, 100757.
[40] D. Son, S. Cho, J. Nam, H. Lee, M. Kim, *Polymers* **2020**, *12*, 1053.
[41] F. De Groot, *Chem. Rev.* **2001**, *101*, 1779.
[42] J. Halim, K. M. Cook, M. Naguib, P. Eklund, Y. Gogotsi, J. Rosen, M. W. Barsoum, *Appl. Surf. Sci.* **2016**, *362*, 406.
[43] J. E. Penner-Hahn, *CCC II* **2003**, *2*, 159.
[44] M.-Q. Zhao, C. E. Ren, Z. Ling, M. R. Lukatskaya, C. Zhang, K. L. Van Aken, M. W. Barsoum, Y. Gogotsi, *Adv. Mater.* **2015**, *27*, 339.
[45] K. A. S. Usman, J. Zhang, D. Y. Hegh, A. O. Rashed, D. Jiang, P. A. Lynch, P. Mota-Santiago, K. L. Jarvis, S. Qin, E. L. Prime, M. Naebe, L. C. Henderson, J. M. Razal, *Adv. Mater. Interfaces* **2021**, *8*, 2002043.
[46] V. Natu, M. Benchakar, C. Canaff, A. Habrioux, S. Célérier, M. W. Barsoum, *Matter* **2021**, *4*, 1224.
[47] N. García-Romeral, M. Keyhanian, Á. Morales-García, F. Illas, *Nanoscale Adv.* **2021**, *3*, 2793.
[48] Y. Yang, K. Hantanasirisakul, N. C. Frey, B. Anasori, R. J. Green, P. C. Rogge, I. Waluyo, A. Hunt, P. Shafer, E. Arenholz, V. B. Shenoy, Y. Gogotsi, S. J. May, *2D Mater.* **2020**, *7*, 025015.
[49] M. R. Lukatskaya, S.-M. Bak, X. Yu, X.-Q. Yang, M. W. Barsoum, Y. Gogotsi, *Adv. Energy Mater.* **2015**, *5*, 1500589.
[50] S.-M. Bak, R. Qiao, W. Yang, S. Lee, X. Yu, B. Anasori, H. Lee, Y. Gogotsi, X.-Q. Yang, *Adv. Energy Mater.* **2017**, *7*, 1700959.
[51] S. Wan, X. Li, Y. Chen, N. Liu, Y. Du, S. Dou, L. Jiang, Q. Cheng, *Science* **2021**, *374*, 96.
[52] D. Kriegner, E. Wintersberger, K. Kawaguchi, J. Wallentin, M. T. Borgström, J. Stangl, *Nanotechnology* **2011**, *22*, 425704.
[53] C. E. Murray, I. Cevdet Noyan, in *Pract. Residual Stress Meas. Methods*, **2013**, *6*, 139.
[54] R. M. Suter, D. Hennessy, C. Xiao, U. Lienert, *Rev. Sci. Instrum.* **2006**, *77*, 123905.
[55] A. A. Bunaciu, E. G. Udristioiu, H. Y. Aboul-Enein, *Crit. Rev. Anal. Chem.* **2015**, *45*, 289.
[56] K. A. S. Usman, J. W. Maina, S. Seyedin, M. T. Conato, L. M. Payawan, L. F. Dumée, J. M. Razal, *NPG Asia Mater.* **2020**, *12*, 58.
[57] F. Liu, A. Zhou, J. Chen, J. Jia, W. Zhou, L. Wang, Q. Hu, *Appl. Surf. Sci.* **2017**, *416*, 781.
[58] O. Mashtalir, M. Naguib, B. Dyatkin, Y. Gogotsi, M. W. Barsoum, *Mater. Chem. Phys.* **2013**, *139*, 147.
[59] A. Feng, Y. Yu, Y. Wang, F. Jiang, Y. Yu, L. Mi, L. Song, *Mater. Des.* **2017**, *114*, 161.
[60] O. Mashtalir, M. Naguib, V. N. Mochalin, Y. Dall'Agnese, M. Heon, M. W. Barsoum, Y. Gogotsi, *Nat. Commun.* **2013**, *4*, 1716.
[61] M. Naguib, R. R. Unocic, B. L. Armstrong, J. Nanda, *Dalton Trans.* **2015**, *44*, 9353.
[62] M. R. Lukatskaya, O. Mashtalir, C. E. Ren, Y. Dall'Agnese, P. Rozier, P. L. Taberna, M. Naguib, P. Simon, M. W. Barsoum, Y. Gogotsi, *Science* **2013**, *341*, 1502.
[63] X. Wang, T. S. Mathis, K. Li, Z. Lin, L. Vlcek, T. Torita, N. C. Osti, C. Hatter, P. Urbankowski, A. Sarycheva, M. Tyagi, E. Mamontov, P. Simon, Y. Gogotsi, *Nat. Energy* **2019**, *4*, 241.
[64] J. Halim, S. Kota, D. Bish, Y. Gogotsi, M. W. Barsourm, *Chem. Mater.* **2016**, *28*, 3507.
[65] X. Mu, D. Wang, F. Du, G. Chen, C. Wang, Y. Wei, Y. Gogotsi, Y. Gao, Y. Dall'Agnese, *Adv. Funct. Mater.* **2019**, *29*, 1902953.
[66] S. Kajiyama, L. Szabova, K. Sodeyama, H. Iinuma, R. Morita, K. Gotoh, Y. Tateyama, M. Okubo, A. Yamada, *ACS Nano* **2016**, *10*, 3334.
[67] S. Célérier, S. Hurand, C. Garnero, S. Morisset, M. Benchakar, A. Habrioux, P. Chartier, V. Mauchamp, N. Findling, B. Lanson, E. Ferrage, *Chem. Mater.* **2019**, *31*, 454.
[68] Y. Lee, S. J. Kim, Y.-J. Kim, Y. Lim, Y. Chae, B.-J. Lee, Y.-T. Kim, H. Han, Y. Gogotsi, C. W. Ahn, *J. Mater. Chem. A* **2020**, *8*, 573.
[69] C. J. Zhang, S. Pinilla, N. McEvoy, C. P. Cullen, B. Anasori, E. Long, S.-H. Park, A. Seral-Ascaso, A. Shmeliov, D. Krishnan, C. Morant, X. Liu, G. S. Duesberg, Y. Gogotsi, V. Nicolosi, *Chem. Mater.* **2017**, *29*, 4848.
[70] S. L. McArthur, *Surf. Interface Anal.* **2006**, *38*, 1380.
[71] B. Philippe, G. J. Man, H. Rensmo, in *Characterization Techniques for Perovskite Solar Cell Materials*, (Eds: M. Pazoki, A. Hagfeldt, T. Edvinsson), Elsevier, Amsterdam **2020**, p. 109.
[72] L.-Å. Näslund, I. Persson, *Appl. Surf. Sci.* **2022**, *593*, 153442.
[73] K. Hantanasirisakul, M. Alhabeb, A. Lipatov, K. Maleski, B. Anasori, P. Salles, C. Ieosakulrat, P. Pakawatpanurut, A. Sinitskii, S. J. May, Y. Gogotsi, *Chem. Mater.* **2019**, *31*, 2941.
[74] L.-Å. Näslund, P. O. Å. Persson, J. Rosen, *J. Phys. Chem. C* **2020**, *124*, 27732.
[75] J. Halim, K. M. Cook, P. Eklund, J. Rosen, M. W. Barsoum, *Appl. Surf. Sci.* **2019**, *494*, 1138.
[76] J. Zhang, N. Kong, D. Hegh, K. A. S. Usman, G. Guan, S. Qin, I. Jurewicz, W. Yang, J. M. Razal, *ACS Appl. Mater. Interfaces* **2020**, *12*, 34032.
[77] M. Mičušík, M. Šlouf, A. Stepura, Y. Soyka, E. Ovodok, M. Procházka, M. Omastová, *Appl. Surf. Sci.* **2023**, *610*, 155351.
[78] Y. Xie, M. Naguib, V. N. Mochalin, M. W. Barsoum, Y. Gogotsi, X. Yu, K.-W. Nam, X.-Q. Yang, A. I. Kolesnikov, P. R. C. Kent, *J. Am. Chem. Soc.* **2014**, *136*, 6385.
[79] F. Yang, D. Hegh, D. Song, J. Zhang, K. A. S. Usman, Z. Wang, P. Zhang, W. Ma, W. Yang, S. Qin, J. M. Razal, *J. Mater. Chem. A* **2021**, *9*, 6393.
[80] G. S. Lee, T. Yun, H. Kim, I. H. Kim, J. Choi, S. H. Lee, H. J. Lee, H. S. Hwang, J. G. Kim, D.-w. Kim, H. M. Lee, C. M. Koo, S. O. Kim, *ACS Nano* **2020**, *14*, 11722.
[81] Y. Wen, T. E. Rufford, X. Chen, N. Li, M. Lyu, L. Dai, L. Wang, *Nano Energy* **2017**, *38*, 368.
[82] S. Wan, X. Li, Y. Wang, Y. Chen, X. Xie, R. Yang, A. P. Tomsia, L. Jiang, Q. Cheng, *Proc. Natl. Acad. Sci. USA* **2020**, *117*, 27154.
[83] C. E. Ren, M.-Q. Zhao, T. Makaryan, J. Halim, M. Boota, S. Kota, B. Anasori, M. W. Barsoum, Y. Gogotsi, *ChemElectroChem* **2016**, *3*, 689.
[84] W. Yang, B. Huang, L. Li, K. Zhang, Y. Li, J. Huang, X. Tang, T. Hu, K. Yuan, Y. Chen, *Small Methods* **2020**, *4*, 2000434.
[85] X. Wang, Z. Wang, J. Qiu, *Angew. Chem., Int. Ed.* **2021**, *60*, 26587.
[86] T. Habib, X. Zhao, S. A. Shah, Y. Chen, W. Sun, H. An, J. L. Lutkenhaus, M. Radovic, M. J. Green, *npj 2D Mater. Appl.* **2019**, *3*, 8.
[87] S. Huang, V. N. Mochalin, *ACS Nano* **2020**, *14*, 10251.
[88] X. Zhao, A. Vashisth, J. W. Blivin, Z. Tan, D. E. Holta, V. Kotasthane, S. A. Shah, T. Habib, S. Liu, J. L. Lutkenhaus, M. Radovic, M. J. Green, *Adv. Mater. Interfaces* **2020**, *7*, 2000845.
[89] X. Zhao, A. Vashisth, E. Prehn, W. Sun, S. A. Shah, T. Habib, Y. Chen, Z. Tan, J. L. Lutkenhaus, M. Radovic, M. J. Green, *Matter* **2019**, *1*, 513.
[90] W. Zaman, R. A. Matsumoto, M. W. Thompson, Y.-H. Liu, Y. Bootwala, M. B. Dixit, S. Nemsak, E. Crumlin, M. C. Hatzell, P. T. Cummings, K. B. Hatzell, *Proc. Natl. Acad. Sci. USA* **2021**, *118*, 2108325118.
[91] J. Yano, V. K. Yachandra, *Photosynth. Res.* **2009**, *102*, 241.
[92] H. Wende, *Rep. Prog. Phys.* **2004**, *67*, 2105.
[93] A. Al-Temimy, B. Anasori, K. A. Mazzio, F. Kronast, M. Seredych, N. Kurra, M.-A. Mawass, S. Raoux, Y. Gogotsi, T. Petit, *J. Phys. Chem. C* **2020**, *124*, 5079.

[94] D. Popmintchev, B. R. Galloway, M.-C. Chen, F. Dollar, C. A. Mancuso, A. Hankla, L. Miaja-Avila, G. O'Neil, J. M. Shaw, G. Fan, S. Ališauskas, G. Andriukaitis, T. Balčiunas, O. D. Mücke, A. Pugzlys, A. Baltuška, H. C. Kapteyn, T. Popmintchev, M. M. Murnane, *Phys. Rev. Lett.* **2018**, *120*, 093002.
[95] N. M. Pirozzi, J. Kuipers, B. N. G. Giepmans, in *Methods in Cell Biology*, Vol. *162*, (Eds: T. Müller-Reichert, P. Verkade), Academic Press, San Diego, CA **2021**, p. 89.
[96] J. E. von Treifeldt, K. L. Firestein, J. F. S. Fernando, C. Zhang, D. P. Siriwardena, C.-E. M. Lewis, D. V. Golberg, *Mater. Des.* **2021**, *199*, 109403.
[97] 199, 109403, Z. Xu, B. Fang, T. Huang, S. Cai, H. Chen, Y. Liu, K. Gopalsamy, W. Gao, C. Gao, *J. Mater. Chem. A* **2017**, *5*, 22113.
[98] P. Bärmann, R. Nölle, V. Siozios, M. Ruttert, O. Guillon, M. Winter, J. Gonzalez-Julian, T. Placke, *ACS Nano* **2021**, *15*, 3295.
[99] T. Tahir, D. Alhashmialameer, S. Zulfiqar, A. M. E. Atia, M. F. Warsi, K. Chaudhary, H. M. El Refay, *Ceram. Int.* **2022**, *48*, 24840.
[100] S.-H. Seok, S. Choo, J. Kwak, H. Ju, J.-H. Han, W.-S. Kang, J. Lee, S.-Y. Kim, D. H. Lee, J. Lee, J. Wang, S. Song, W. Jo, B. M. Jung, H. G. Chae, J. S. Son, S.-Y. Kwon, *Nanoscale Adv.* **2021**, *3*, 517.
[101] C. Peng, P. Wei, X. Chen, Y. Zhang, F. Zhu, Y. Cao, H. Wang, H. Yu, F. Peng, *Ceram. Int.* **2018**, *44*, 18886.
[102] X. Luo, L. Zhu, Y.-C. Wang, J. Li, J. Nie, Z. L. Wang, *Adv. Funct. Mater.* **2021**, *31*, 2104928.
[103] P. Yan, L. Ji, X. Liu, Q. Guan, J. Guo, Y. Shen, H. Zhang, W. Wei, X. Cui, Q. Xu, *Nano Energy* **2021**, *86*, 106139.
[104] J. Shen, G. Liu, Y. Ji, Q. Liu, L. Cheng, K. Guan, M. Zhang, G. Liu, J. Xiong, J. Yang, W. Jin, *Adv. Funct. Mater.* **2018**, *28*, 1801511.
[105] 28, 1801511, M. Dahlqvist, J. Halim, E. J. Moon, J. Lu, B. C. Hosler, E. a. N. Caspi, S. J. May, L. Hultman, P. Eklund, J. Rosén, M. W. Barsoum, *J. Appl. Phys.* **2015**, *118*, 094304.
[106] B. Anasori, Y. Xie, M. Beidaghi, J. Lu, B. C. Hosler, L. Hultman, P. R. C. Kent, Y. Gogotsi, M. W. Barsoum, *ACS Nano* **2015**, *9*, 9507.
[107] Z. Xu, Y. Zhang, H. Dai, Y. Wang, Y. Ma, S. Tan, B. Han, *J. Ind. Eng. Chem.* **2022**, *114*, 536.
[108] Y. Jiang, X. Xie, Y. Chen, Y. Liu, R. Yang, G. Sui, *J. Mater. Chem. C* **2018**, *6*, 8679.
[109] A. Rozmyslowska-Wojciechowska, E. Karwowska, M. Gloc, J. Wozniak, M. Petrus, B. Przybyszewski, T. Wojciechowski, A. M. Jastrzebska, *Materials* **2020**, *13*, 4587.
[110] 13, 4587, T. Xia, S. Ghosh, J. Wang, S. D. Rawson, P. J. Withers, I. A. Kinloch, S. Barg, *2D Mater.* **2021**, *8*, 025022.
[111] Q. Yang, H. Yin, T. Xu, D. Zhu, J. Yin, Y. Chen, X. Yu, J. Gao, C. Zhang, Y. Chen, Y. Gao, *Small* **2020**, *16*, 1906814.
[112] X. Mi, Z. Su, Y. Fu, S. Li, A. Mo, *Biomed. Mater.* **2022**, *17*, 035002.
[113] R. Nie, Y. Sun, H. Lv, M. Lu, H. Huangfu, Y. Li, Y. Zhang, D. Wang, L. Wang, Y. Zhou, *Nanoscale* **2022**, *14*, 8112.
[114] J. Zhang, Y. Fu, A. Mo, *Int. J. Nanomed.* **2019**, *14*, 10091.
[115] S. Pan, J. Yin, L. Yu, C. Zhang, Y. Zhu, Y. Gao, Y. Chen, *Adv. Sci.* **2020**, *7*, 1901511.
[116] S. Feng, Y. Yi, B. Chen, P. Deng, Z. Zhou, C. Lu, *ACS Appl. Mater. Interfaces* **2022**, *14*, 36060.
[117] V. Bayram, M. Ghidiu, J. J. Byun, S. D. Rawson, P. Yang, S. A. McDonald, M. Lindley, S. Fairclough, S. J. Haigh, P. J. Withers, M. W. Barsoum, I. A. Kinloch, S. Barg, *ACS Appl. Energy Mater.* **2019**, *3*, 411.
[118] S. D. Rawson, V. Bayram, S. A. McDonald, P. Yang, L. Courtois, Y. Guo, J. Xu, T. L. Burnett, S. Barg, P. J. Withers, *ACS Nano* **2022**, *16*, 1896.
[119] X. Pan, J. Yu, X. Lu, Q. Wang, X. Ma, S. Cao, Y. Ni, *J. Colloid Interface Sci.* **2022**, *623*, 1151.
[120] L. P. Djukic, I. Herszberg, W. R. Walsh, G. A. Schoeppner, B. Gangadhara Prusty, D. W. Kelly, *Composites, Part A* **2009**, *40*, 553.
[121] L. E. Crica, J. Wengenroth, H. Tiainen, M. Ionita, H. J. Haugen, *J. Biomater. Sci., Polym. Ed.* **2016**, *27*, 805.
[122] G. Chen, W. Yu, D. Singh, D. Cookson, J. Routbort, *J. Nanopart. Res.* **2008**, *10*, 1109.
[123] A. Radlinski, M. Mastalerz, A. Hinde, M. Hainbuchner, H. Rauch, M. Baron, J. Lin, L. Fan, P. Thiyagarajan, *Int. J. Coal Geol.* **2004**, *59*, 245.
[124] T. Pott, P. Méléard, *Phys. Chem. Chem. Phys.* **2009**, *11*, 5469.
[125] T. Zhou, Y. Yu, B. He, Z. Wang, T. Xiong, Z. Wang, Y. Liu, J. Xin, M. Qi, H. Zhang, X. Zhou, L. Gao, Q. Cheng, L. Wei, *Nat. Commun.* **2022**, *13*, 4564.
[126] H. Shin, W. Eom, K. H. Lee, W. Jeong, D. J. Kang, T. H. Han, *ACS Nano* **2021**, *15*, 3320.
[127] T. Zhou, C. Zhao, Y. Liu, J. Huang, H. Zhou, Z. Nie, M. Fan, T. Zhao, Q. Cheng, M. Liu, *ACS Nano* **2022**, *16*, 12013.
[128] 2022, 16, 12013, C. Wu, Y. Wang, A. P. Tomsia, M. Li, E. Saiz, S. Fang, R. H. Baughman, L. Jiang, Q. Cheng, *Nat. Commun.* **2020**, *11*, 2077.
[129] K. A. S. Usman, J. Zhang, S. Qin, Y. Yao, P. A. Lynch, P. Mota-Santiago, M. Naebe, L. C. Henderson, D. Hegh, J. M. Razal, *J. Mater. Chem. A* **2022**, *10*, 4770.

Jizhen Zhang received his Ph.D. at Deakin University in 2020 and won the Chinese Government Award for Outstanding Self-financed Students Abroad. He is currently an associate research fellow at the Institute for Frontier Materials (IFM), Deakin University and enrolled as a research scientist in the Materials Characterisation and Modelling Group at the Manufacturing of the Commonwealth Scientific and Industrial Research Organisation (CSIRO). He is closely working with Prof. Joselito M. Razal and Prof. Peter A. Lynch in exploring fiber-based energy storage devices using 2D materials, including $Ti_3C_2T_x$ MXene, and developing a lab-scale X-ray facility "InSitX" for fast and in situ SAXS/WAXS characterization.

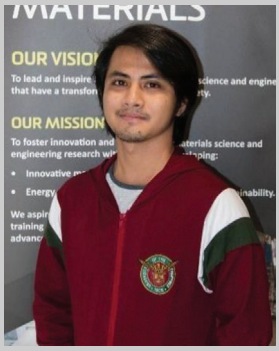

Ken Aldren S. Usman is currently an associate research fellow at the Institute for Frontier Materials (IFM), Deakin University, under the supervision of Prof. Joselito A. Razal and Dr. Dylan Hegh. His research interests include synthesis and surface modification of nanomaterials, and processing of functional architectures. His recently concluded Ph.D. work focused on developing structurally fortified and bioinspired $Ti_3C_2T_x$ MXene-based materials with uncompromised electrical and electrochemical performance.

Joselito M. Razal is the Director of the ARC Research Hub for Future Fibres and the Leader of the Future Fibres Group at the Institute for Frontier Materials, Deakin University. He is best known for his research on functional and sustainable fibrous materials for flexible energy storage, energy conversion, and energy harvesting systems. For his pioneering works, he was awarded several fellowships including ARC APD Fellowship at the University of Wollongong (2009), ARC Future Fellowship at Deakin University (2013) and Endeavour Executive Fellowship at Cornell University (2019).